Mon. Not. R. Astron. Soc. **000**, 000–000 (0000) Printed 2 July 2018 (MN LATEX style file v2.2)

Neutron star bulk viscosity, "spin-flip" and GW emission of newly born magnetars

S. Dall'Osso[1,⋆], L. Stella[2], C. Palomba[3]
[1] *Department of Physics & Astronomy, Stony Brook University, Stony Brook 11579 NY, USA*
[2] *INAF - OAR, via di Frascati 33, 00078, Monte Porzio Catone, Roma, Italy*
[3] *INFN, Sezione di Roma, P.le A. Moro, 2, I-00185 Roma, Italy*

2 July 2018

ABSTRACT
The viscosity-driven "spin-flip" instability in newly born magnetars with interior toroidal magnetic fields is re-examined. We calculate the bulk viscosity coefficient (ζ) of cold, $npe\mu$ matter in neutron stars (NS), for selected values of the nuclear symmetry energy and in the regime where β-equilibration is slower than characteristic oscillation periods. We show that: i) ζ is larger than previously assumed and the instability timescale correspondingly shorter; ii) for a magnetically-induced ellipticity $\epsilon_B \lesssim 4\times10^{-3}$, typically expected in newborn magnetars, spin-flip occurs for initial spin periods $\lesssim 2-3$ ms, with some dependence on the NS equation of state (EoS).
We then calculate the detectability of GW signals emitted by newborn magnetars subject to "spin-flip", by accounting also for the reduction in range resulting from realistic signal searches. For an optimal range of $\epsilon_B \sim (1-5)\times10^{-3}$, and birth spin period $\lesssim 2$ ms, we estimate an horizon of $\gtrsim 4$ Mpc, and $\gtrsim 30$ Mpc, for Advanced and third generation interferometers at design sensitivity, respectively. A supernova (or a kilonova) is expected as the electromagnetic counterpart of such GW events.
Outside of the optimal range for GW emission, EM torques are more efficient in extracting the NS spin energy, which may power even brighter EM transients.

Key words: dense matter – equation of state – stars: magnetar – gravitational waves – stars: magnetic fields – (stars:) supernovae: general

1 INTRODUCTION

The first detections of GWs from binary black holes (BH; Abbott et al. 2016, Abbott et al. 2017a) and from a binary NS merger (Abbott et al. 2017d) have opened a new era in physics and astronomy. Newly born magnetars have long been discussed as a class of compact objects of potential relevance for current and future GW detectors (Cutler 2002, Stella et al. 2005, Dall'Osso et al. 2009, Corsi & Meszaros 2009, Dall'Osso et al. 2015).

The ability of newborn magnetars to emit a distinctive GW signal, the properties of such signals, and their rate of occurrence, are sensitive to the NS properties; therefore, they hold the potential to probe the physics of NS interiors. Cutler (2002) first pointed out that millisecond spinning NS with predominantly toroidal interior B-fields, e.g. magnetars, may be subject to a secular instability first discussed by Jones (1976), which favors intense GW emission. Schematically[1], a strong toroidal field deforms the NS shape into a prolate ellipsoid, which undergoes freebody precession. Dissipation of the precession energy, due to the NS interior viscosity, will drive the symmetry (magnetic) axis of the ellipsoid orthogonal to the spin axis, thus maximizing GW emission efficiency. This is often referred to as[2] "spin-flip instability"; the *prolate* shape of the ellipsoid, induced by a strong *toroidal* magnetic field in the NS core, is essential for the instability.

The B-field strength in magnetar cores can only be inferred from observations of the galactic population. Based on the energetics of the Dec 27, 2004 Giant Flare of the Soft Gamma Repeater SGR 1806-20, Stella et al. (2005) derived a lower limit $\sim 10^{16}$ G for the volume-averaged B-field *at birth*. Makishima et al. (2014), based on the possible precession of the Anomalous X-ray Pulsar 4U 0142+61, estimated B $\sim 10^{16}$ G at $\sim 10^4$ yrs age. Such magnetic field in the core of newborn magnetars would give rise to GW signals detectable from well beyond the Milky Way.

⋆ contact address: sim.dall@gmail.com
[1] see Cutler (2002) and Jones (1976) for more details.
[2] Even though, in the observer's frame, it is the magnetic symmetry axis that flips.

Key to strong GW emission is that flipping of the symmetry axis be fast compared to other mechanisms like, e.g. magnetic dipole radiation, that tap the same energy reservoir as GWs, *i.e.* the NS spin. Thus, an effective source of viscosity is crucial. To further study this scenario, Dall'Osso et al. (2009) considered bulk viscosity in pure *npe* NS matter soon after birth, at temperatures $\sim 10^{10}$ K, when the NS crust has not yet formed.

These authors concluded that: i) for birth spin $\sim$ 1-3 ms, the instability is sufficiently fast if the interior B-field is[3] $\mathrm{B_{int,16}} \lesssim 4$ and the exterior dipole $\mathrm{B_{d,14}} \lesssim 5$; ii) GW signals are detectable with Advanced LIGO/Virgo from Virgo cluster distances. Given an estimated magnetar formation rate ~ 1 yr^{-1} within that volume, this may lead to an interesting rate of detectable events, in particular for $B_{\rm int,16} \gtrsim 1$, $B_{\rm dip,14} < 3$, and birth spin periods < 2.5 ms.

Here we improve on previous work in several ways: in Sec. 2 we calculate the bulk viscosity coefficient of *npeμ* matter, for three representative choices of the NS EoS, showing that it is generally larger than previously assumed. In passing, we address doubts raised about the effectiveness of bulk viscosity. In Sec. 3 we summarize the formalism used to model spin-flip as a consequence of viscous dissipation of freebody precession, and calculate numerically the time evolution of the tilt angle of the magnetic axis, along with the corresponding GW luminosity. In Sec. 4, using our new results, we re-asses the detectability of newborn magnetars with current and future GW detectors, and further comment on perspectives for the detection of associated EM signals.

2 BULK VISCOSITY IN THE NS CORE

Fluid bulk viscosity is due to pressure/density variations from equilibrium. In a precessing NS, such fluctuations are excited at the precession frequency. In β-stable NS matter, pressure depends on the local density *and* charged particle fraction: when a fluid element is displaced from equilibrium, the ensuing compression will activate β-reactions, to establish a new pressure and chemical equilibrium. Bulk viscosity is thus characterised by two timescales: the perturbation period, $T_p = 2\pi/\omega$, equal to the precession period, and the relaxation timescale $\tau_\beta = 2\pi/\omega_\beta$, on which chemical equilibrium is restored. For *npe* matter, the bulk viscosity coefficient is[4] (Lindblom & Owen 2002)

$$\mathrm{Re}(\zeta) \equiv \frac{n_b \tau_\beta \left(\frac{\partial P}{\partial x}\right)_{n_b} \frac{dx}{dn}}{1+(\omega\tau_\beta)^2} = \frac{z}{1+z^2}\frac{n_b}{\omega}\left(\frac{\partial P}{\partial x}\right)_{n_b}\frac{dx}{dn_b}\,. \quad (1)$$

where P, n_b are the total pressure and baryon density, $z = \omega\tau_\beta$ and $x = n_p/n_b$ the proton fraction. Eq. (1) highlights the dependence of bulk viscosity on the perturbation frequency, chemical composition, density and pressure profiles of the NS structure.

[3] From here on, $Q_n \equiv Q/10^n$.

[4] Eq. 1 is valid for any fluid with relativistic components. For practical purposes, in the case of *npeμ* matter, we will adopt a slightly different expression which is derived from (1).

The different regimes – Eq. (1) has two main regimes of ζ as a function of z:

i) $z \ll 1$, "low frequency" limit. Chemical equilibrium is established quickly compared to the perturbation period (T_p). Thus, deviations from chemical equilibrium cannot grow much and energy losses remain very limited, resulting in a small bulk viscosity coefficient, which scales like $\zeta \propto z$;

ii) $z \gg 1$, "high frequency" limit. Chemical imbalance is erased over a time much longer than the perturbation period. During each cycle, deviations from chemical equilibrium grow *almost* freely: the small dissipation due to β-reactions only builds up in a large number of cycles, eventually damping the perturbation. In this regime $\zeta \propto z^{-1}$.

These two regimes join smoothly around $z \sim 1$, where the bulk viscosity coefficient $\zeta(z)$ reaches a maximum.

Standard expression – $z \gg 1$ is typically the relevant regime in NS (e.g. Haensel, Levenfish & Yakovlev 2000, 2001, Lindblom & Owen 2002, Dall'Osso et al. 2009), unless $T > 10^{10}$ K. In particular, assuming a NS made of pure *npe* matter, and treating each particle species as a fluid of non-interacting, fully degenerate fermions, the standard expression for the bulk viscosity coefficient (Sawyer 1989) can be derived from Eq. 1 for $z \gg 1$

$$\zeta^{(\rm std)} \approx 6\times 10^{-59}\rho^2 T^6 \omega^{-2}\,. \quad (2)$$

Eq. 2 can be improved in two ways: *a)* a more realistic description of NS matter, which accounts for the interactions among baryons, by specifying the NS EoS; *b)* the inclusion of additional particles, expected to appear in the NS core at large densities (e.g., Haensel et al. 2000, Lindblom & Owen 2002). Muons will be first produced in β-reactions once the electron Fermi energy exceeds the muon rest-mass $\approx$ 105 MeV. The exact density threshold for muon production depends on the NS EoS and has a typical value $\rho \lesssim 2.3\times 10^{14}$ g cm^{-3}. We will not consider further particles, that might appear in the core at $\rho > 8\times 10^{14}$ g cm^{-3}.

2.1 Nuclear symmetry energy

Baryon interactions in the NS EoS are described in terms of $E_N(n_b, x)$, the nucleon energy per baryon, at baryon number density $n_b = n_n + n_p$. If $\mathrm{E}_N(n_b, 0)$ is the energy of pure neutron matter and $E_N(n_b, 1/2)$ the energy of symmetric matter, then the former exceeds the latter by the symmetry energy, $S_0(n_b)$. For intermediate x-values, the excess energy is obtained interpolating between these two limits

$$\mathrm{E}_N(n_b, x) \approx \mathrm{E}_N(n_b, 1/2) + S_0(n_b)(1-2x)^2\,. \quad (3)$$

$S_0(n_b)$ has a kinetic and a potential energy component

$$S_0(u) = S_k u^{2/3} + S_v u^\gamma\,, \quad (4)$$

the latter incorporating baryons interactions. In Eq. 4, $u = n_b/n_s$, $n_s \approx 0.16$ fm^{-1} is the baryon number density at the nuclear saturation density $\rho_s \approx 2.7\times 10^{14}$ g cm^{-3}, $S_k = 17$ MeV and $S_k + S_v = S_0(u_s)$. The index $\gamma \sim 0.2 - 1$ (Steiner et al. 2010) parametrizes the uncertain scaling of the potential energy with density. Eq. 4 is often written as $S_0(n_b) = S_\nu\,(n_b/n_s)^\Gamma$, where $S_\nu = S_k + S_v \sim 30 - 34$ MeV positively correlates with $\Gamma \sim 0.45 - 0.7$ (Lattimer & Prakash 2016). Here, we consider three representative choices of (S_v, γ) that span the range of uncertainty on

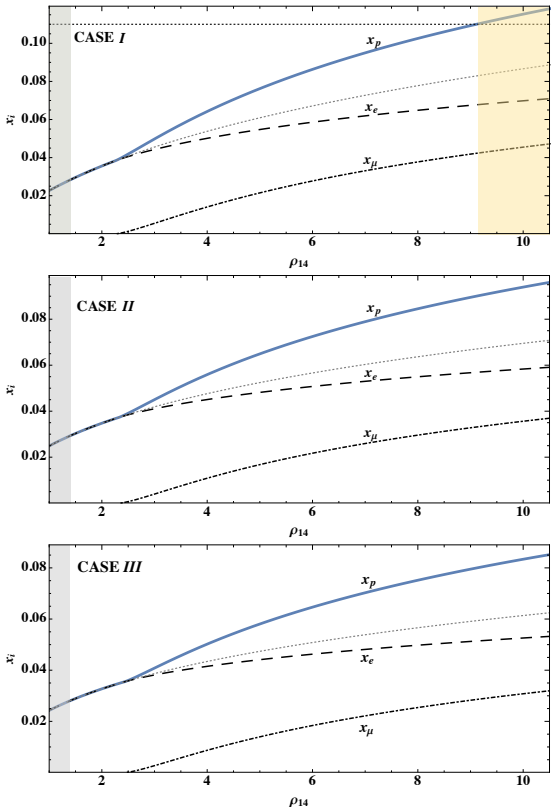

Figure 1. Proton, electron and muon fractions for the three cases in Tab. 1. *Upper Panel*: the horizontal dotted line is the x_p threshold for direct Urca reactions. It is not reached in cases II and III. In the yellow area direct Urca reactions are allowed, hence our calculations should be modified. The grey area on the left corresponds to densities of the NS crust.

both parameters: chosen values are reported in Tab. 1. Case I gives a relatively stiff EoS approximating the APR EoS (Akmal, Pandharipande & Ravenhall 1998). Cases II and III give a progressively softer EoS, consistent with a NS maximum mass $\gtrsim 2M_\odot$ (e.g. Demorest et al. 2010).

2.2 Charged particle fraction

Accounting for baryon interactions increases the charged particle fraction with respect to the simple case with no interactions.

Case 1. npe **matter** – the total energy per baryon inside a NS includes, besides E_N, the energy of relativistic electrons, $\mathrm{E}_e = 3/4 x E_{F_e} = (3/4)\hbar c x (3\pi^2 n_b x)^{1/3}$, with $x = x_e = x_p$ due to charge neutrality. The equilibrium composition is obtained by minimizing the total energy with respect to x, $\partial\left[E_N(n_b,x) + E_e(n_b,x)\right]/\partial x = 0$, which is equivalent to imposing the equality of the chemical potentials, $\mu_e = \mu_n - \mu_p$

$$\hbar c \left(3\pi^2 n_b x\right)^{1/3} = -\frac{\partial E_N}{\partial x} = 4 S_\nu \left(\frac{n_b}{n_s}\right)^\Gamma (1-2x)\,. \qquad (5)$$

Solving Eq. 5 gives the proton fraction in the NS core: for example, at the nuclear saturation density, $x(n_s) \approx 0.04$ for all EoS considered, as opposed to $x(n_s) \approx 0.006$ obtained in the non-interacting case.

Table 1. Different choices for the symmetry energy S_ν and power-law index γ. Case I matches closely the results for the APR EoS. Cases II and III are for illustration purposes.

CASE	S_v[MeV]	γ	S_ν[MeV]	Γ
I	15.5	1/2	32.5	0.59
II	14.5	1/3	31.5	0.525
III	13.5	1/4	30.5	0.503

Case 2. $npe\mu$ **matter** – : the appearence of muons introduces new constraints. First, the electron and muon chemical potentials must be equal. Second, x_e and x_p will appear as different variables in Eq. 5, since now x_p must equal the sum of the electron and muon fractions. The e, μ and p fractions are determined from

$$\begin{aligned} \mu_e &= \mu_n - \mu_p \\ \mu_\mu &= \mu_e \\ x_p &= x_e + x_\mu\,. \end{aligned} \qquad (6)$$

The profiles $x_p(n_b), x_e(n_b)$ and $x_\mu(n_b)$, corresponding to the three EoS's of Tab. 1 are shown Fig. 1. The threshold for muons production is $\rho_\mu \approx 2.5 \times 10^{14}$ g cm^{-3}: below ρ_μ, $x_\mu = 0$ while $x_p = x_e$ is determined by Eq. 5. Where muons appear, the proton fraction is increased. Accordingly, the threshold for the onset of direct URCA reactions is reached at a somewhat lower density ($\gtrsim 9 \times 10^{14}$ g cm^{-3}).

2.3 Relaxation timescale

The relaxation timescale, in the same approximation that gives Eq. 2, is (Reisenegger & Goldreich 1992)

$$\tau_\beta^{(\mathrm{old})} = \frac{3 n_c}{\lambda E_{F_n}} \approx 6.9 \text{ s } (\rho/\rho_\mathrm{n})^{2/3} T_{10}^{-6}\,, \qquad (7)$$

where λ is related to the emissivity of modified Urca reactions and E_{F_n} is the neutron Fermi energy. Including $S(n_b, x)$ decreases τ_β, which in turn increases ζ compared to Eq. 2. In order to derive the relaxation timescale in this case let us assume e.g., a density perturbation in a fluid element, which will thus find itself out of chemical equilibrium by the amount $\delta\mu = \mu_n - \mu_p - \mu_e$. This is related to δn_c, the deviation of the charged particle density from its equilibrium value (Eq. 5). β-reactions will be activated, in order to bring n_c to its new equilibrium value and restore chemical equilibrium ($\delta\mu = 0$). The relaxation timescale is, as usual, $\tau_\beta = \delta n_c / \delta\Gamma$, where $n_c = n_p = n_e$, and $\delta\Gamma = \lambda\delta\mu$ is[5] the difference in the rates between direct and inverse β-reactions. Perturbing Eq. 5 with respect to x, we get

$$\tau_\beta \equiv \frac{3 n_c}{\lambda\left[E_{F_n} + 24 S_\nu\ x (n_b/n_s)^\gamma\right]}\,. \qquad (8)$$

which generalizes Eq. (7). The symmetry energy term in the denominator is typically $\gtrsim 0.5\ \mathrm{E}_{F_n}$, which reduces τ_β in npe by a factor 1.5 compared to $\tau_\beta^{(\mathrm{old})}$.
Allowing for the presence of muons, and accounting for the

[5] Under the assumption that $\delta\mu \ll kT$.

contribution of the proton branch of different β-reactions, provides another factor ~ 2 reduction (Haensel et al. 2001). We thus conclude that $\tau_\beta \simeq 1/3\tau_\beta^{(\rm old)}$ for $npe\mu$ matter.

2.4 Total energy and pressure profile

The total energy per baryon, for $npe\mu$ matter, is $\mathrm{E}_T(n_b, x_p) = E_N(n_b, x_p) + 3/4 x_e E_e(n_b, x_p) + 3/4 x_\mu E_\mu(n_b, x_p)$, where E_μ is the equivalent of E_e. The total pressure is $P(n_b, x_p) = P_N(n_b, x_p) + P_e + P_\mu$, where P_e, P_μ are the partial pressures of the free lepton gases. The nucleon pressure is defined as

$$P_N(n_b, x_p) = n_b^2 \frac{\partial E_{\rm N}(n_b, x_p)}{\partial x} \,. \qquad (9)$$

$p = n^2 \partial \left[E(n,x) + E_e(n,x)\right]/\partial x$. Summing P_e and P_μ to Eq. 9 gives the total pressure as a function on n_b and x, needed to calculate $(\partial P/\partial x)_n$ in Eq. 1.

2.5 Bulk viscosity coefficient of $npe\mu$ matter

When several particles species are present, the formulation by Haensel et al. (2001) turns out to be more practical to calculate ζ than that of Eq. 1. We write the total bulk viscosity as the sum of partial bulk viscosities[6] due to each of the channels for β-reactions. Thus, $\zeta = \zeta_{ne} + \zeta_{pe} + \zeta_{n\mu} + \zeta_{p\mu}$, where

$$\zeta_{Nl} = \frac{\lambda_{Nl}}{\omega^2} \left|\frac{\partial P}{\partial x}\right|_{n_b} \frac{dx}{dn_b} = \frac{|\lambda_{Nl}|}{\omega^2} C_l^2 \,, \qquad (10)$$

Nl standing for each nucleon/lepton couple. The term $C_l \equiv n_b \partial \eta_l / \partial n_b$, where $\eta_l = \mu_n - \mu_p - \mu_l$ is the chemical potential imbalance of leptons, and the λ's for each branch of modified URCA reactions are given by Haensel et al. (2001). The neutron/proton chemical potentials are $\mu_{n,p} = \partial \left(n_b E_N\right)/\partial n_{n,p}$. For the leptons, $\mu_l = \left(m_l^2 c^4 + p_{Fl}^2 c^2\right)^{1/2}$, where $p_{Fl} = \hbar \left(3\pi^2 n_l\right)^{1/3}$ is the Fermi momentum.
With these definitions, C_l becomes (Haensel et al. 2000)

$$\begin{aligned} C_l &= -n_b \frac{\partial^2 E_N(n_b, x_p)}{\partial n_b \partial x_p} - \frac{c^2 p_{Fl}^2}{3\mu_l} = \\ &= (1 - 2x_p)\, n_b \frac{d}{dn_b}\left(\frac{\mu_l}{1 - 2x_p}\right) - \frac{c^2 p_{Fl}^2}{3\mu_l} \,, \end{aligned} \qquad (11)$$

where Eq. 4 has been used in the last step. We adopted Eq. 11 to calculate the bulk viscosity coefficient of $npe\mu$ matter, for the three EoS's discussed in Sec. 2.1. The results are shown in Fig. 2: for each case, the blue curve shows the run of ζ with density, compared with its value in the absence of muons, and with the value given by Eq. 2. More details are given in the caption.

In all three cases, the resulting bulk viscosity coefficient is greater than the standard one at all densities: their ratio decreases slightly with density for EoS's II and III, while it is constant for EoS I (above the threshold for the appearence of muons). Assuming a NS with a 12 km radius and 1.4 $\mathrm{M}_\odot$ mass, the density-averaged values of ζ for the three EoS's considered here are, respectively, $\sim 5, 3$ and 2 times larger than the density-averaged value of Eq. 2. These ratios represent a convenient parametrization of the effective increase of NS bulk viscosity, for the EoS's and chemical compositions considered here, and will be adopted in the following.

[6] For $\tau_\beta > T$.

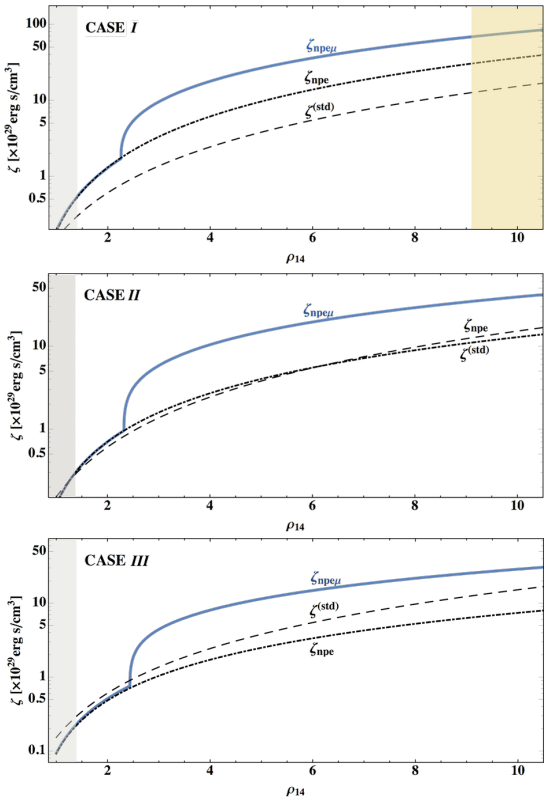

Figure 2. Bulk viscosity coefficient for $npe\mu$ NS matter (blue), for the three cases of Sec. 2.1. The curves marked ζ_{npe} represent the coefficient calculated without muons, those marked $\zeta^{(\rm std)}$ are from the "standard" expression (Eq. 2). The grey and yellow shaded areas are as in Fig. 1. From top to bottom, the density-averaged value of ζ is about 5, 3 and 2 times larger than that derived from Eq. 2.

3 "SPIN-FLIP"

We can now calculate the time evolution of the tilt angle in newborn magnetars. Most details were worked out by Dall'Osso et al. (2009), based on Mestel & Takhar (1972; see also Lasky & Glampedakis 2016).

NS cooling – We consider modified Urca cooling, that is simply described as (e.g. Page et al. 2006)

$$T_{10}(t) = \left(\frac{t}{20\ \mathrm{s}} + \frac{1}{T_{i,10}^6}\right)^{-1/6} \,, \qquad (12)$$

$T_{10} = T/10^{10}$K being the NS temperature and assuming $\mathrm{T}_{i,10} \gtrsim 3$. Eq. 12 describes hot NS where neither protons nor neutrons are superfluid. Protons become superconducting below $\mathrm{T}_{cp,10} \sim 5$, or $t \approx 10^3$ s, while neutrons likely become superfluid at much lower T (and later times; e.g. Page et al. 2011). The transition to proton superconductivity reduces progressively the neutrino emissivity, as T drops below

T_{cp}: however, (12) remains approximately valid as long as $T/T_{cp} \gtrsim 0.7$ (cf. Haensel et al. 2001), *i.e.* up $t \sim 10^4$ s.

Magnetically-induced ellipticity – As a first approximation, the NS magnetically-induced ellipticity is of the order of the ratio of magnetic to gravitational binding energy,

$$\epsilon_B \sim 4 \times 10^{-4} B_{t,16}^2 R_{12}^4 / M_{1.4}^2 \,, \tag{13}$$

where $B_{t,16}$ is the volume-averaged *toroidal* field strength in units of 10^{16} G, R_{12} the NS radius in units of 12 km and $M_{1.4}$ the NS mass, in units of 1.4 $M_\odot$. Corrections due to the magnetic field geometry in the NS interior can lead to substantially larger deformations at a given B-field strength (Bonazzola & Gourgoulhon 1996, Mastrano et al. 2011, Akgün et al. 2013, Dall'Osso et al. 2015). In particular, the toroidal-to-poloidal field ratio is an unknown parameter that can be very large in the core of non-barotropic NS (Braithwaite 2009, Akgün et al. 2013, Ciolfi & Rezzolla 2013). Given these uncertainties, we will adopt $\epsilon_B \approx 10^{-3}$ as a reference value[7] of ϵ_B for a $\sim 10^{16}$ G toroidal B-field in the NS core. Calling χ the tilt angle of the magnetic symmetry axis to the spin axis, the freebody precession frequency will be $\omega = \Omega \epsilon_B \cos\chi$, with Ω the NS spin frequency.

3.1 Energy dissipation

The energy dissipation rate due to bulk viscosity is

$$\dot{\mathrm{E}}_{\rm diss} \equiv \int \zeta |\nabla \cdot \delta \mathbf{v}|^2 \sim \omega^2 \int \zeta \, (\Delta\rho/\rho)^2 \, dV \,, \tag{14}$$

where $\Delta\rho = \delta\rho + \boldsymbol{\xi} \cdot \nabla\rho = -\rho_0 \nabla \cdot \boldsymbol{\xi}$ is the Lagrangian density perturbation due to the precessional motion, $\delta\rho$ the corresponding Eulerian perturbation, $\boldsymbol{\xi}$ the displacement field and $\delta\boldsymbol{v} = \partial_t \boldsymbol{\xi}$ the velocity perturbation.

Fluid compression – Dall'Osso et al. (2009) approximated $\Delta\rho \approx \delta\rho$, adopting $\delta\rho$ as derived by Mestel & Takhar (1972). Lasky & Glampedakis (2016) argued that this approximation only holds if $\omega\tau_\beta < 1$ whereas, if $\omega\tau_\beta > 1$, β-reactions would have no time to occur in one precession cycle, leaving the charged particle fraction unchanged, $\Delta x = 0$; since, to first order in the perturbation, the fluid compression $\nabla \cdot \boldsymbol{\xi} \propto \Delta\rho \propto \Delta x$, this[8] would give $\Delta\rho = 0$, thus quenching bulk viscosity and preventing spin-flip.
By imposing $\omega\tau_\beta \leq 1$, and using the spin-flip timescale (Eq. 16), Lasky & Glampedakis (2016) derived a maximum ellipticity $\epsilon_{\rm sf} \approx 5 \times 10^{-3} \rho_{15} / P_{\rm ms}^2$ for spin-flip to operate ($\mathrm{P_{ms}}$ is the spin period in milliseconds). Repeating their argument with our updated values $\tau_\beta = 1/3\tau_\beta^{\rm (old)}$ and $\zeta = A\zeta^{\rm (std)}$ (Sec. 2.1 and 2.5), we find $\epsilon_{\rm sf}^{\rm (new)} = A\epsilon_{\rm sf} \approx 1.5 \times 10^{-2} (\mathrm{A}/3) \rho_{15} / P_{\rm ms}^2$. The mechanism can thus operate on a wider range of ellipticities than previously suggested: constraints on ϵ_B based on short GRB observations should be accordingly revised.

[7] For example, the twisted-torus used in Dall'Osso et al. 2015 has $\epsilon_B \approx 0.9 \times 10^{-3} B_{t,16}^2$, for the same mass and radius used here.
[8] This proportionality holds strictly to first-order (Mestel & Takhar 1972). Studying higher-order terms, Lander & Jones (2017) found that fluid compressibility remains high even as Δx is reduced. Our estimates may thus be regarded as conservative.

The above argument is still approximate, since it (i) uses the simple scaling (16), (ii) has an explicit dependence on ρ and (iii) assumes a sharp cut-off of bulk viscosity at $\omega\tau_\beta = 1$. To improve on these points we use the definition of the dissipation timescale (Eq. 15), integrating it over the NS density profile, and introduce a slight modification in the treatment of fluid compressibility. First note that τ_β defines the characteristic timescale for β-reactions in a perturbed fluid element. Because a large number of such reactions per unit volume ($\sim \delta n_c$) must occur in the time τ_β, a fraction $\sim t/\tau_\beta$ of those reactions must occur in a time interval $t < \tau_\beta$, causing some energy dissipation. Consider now a perturbation with the period $T_p < \tau_\beta$. The charged particle fraction will change by an amount that is $\sim T_p/\tau_\beta$ times smaller than when $T_p > \tau_\beta$, and we expect $\Delta\rho$ to be $\sim T_p/\tau_\beta$ smaller than in the long timescale regime, where it was $\approx \delta\rho$. Thus, when $\tau_\beta > T_p$ we assume the relation $\Delta\rho \approx \delta\rho(T_p/\tau_\beta)$: the decreasing efficiency of β-reactions provides a force that opposes compression but, as long as $T_p \approx \tau_\beta$, cannot prevent it altogether.
To summarize, depending on the bulk viscosity regime we will write: *a)* $\Delta\rho \approx \delta\rho$ ($\omega\tau_\beta \leq 1$, highly compressible fluid); *b)* $\Delta\rho = \delta\rho(T_p/\tau_\beta)$ in the opposite limit ($\omega\tau_\beta > 1$). Note that, because the integral in (14) contains the square of $\Delta\rho$, energy dissipation becomes quickly negligible as $\tau_\beta > T_p$. Thus, our expression models the onset of fluid incompressibility as a smooth, yet fast transition that occurs, as the NS cools, in a narrow region around $\omega\tau_\beta \gtrsim 1$.

3.2 Dissipation timescale

The energy dissipation timescale is (Ipser & Lindblom 1991)

$$\tau_{\rm diss} \equiv \frac{2E_{\rm pre}}{\dot{E}_{\rm diss}} = \frac{I}{\epsilon_B} \frac{1}{\displaystyle\int \zeta \left(\frac{\Delta\rho}{\rho}\right)^2 dV} \tag{15}$$

where, to first order in ϵ_B, the freebody precession energy is $\mathrm{E_{pre}} = 1/2 I \Omega^2 \epsilon_B \cos^2\chi = 1/2 I \omega^2 \epsilon_B^{-1}$ (Dall'Osso et al. 2009). A simple dimensional analysis of (15) gives the scaling of $\tau_{\rm diss}$ with the NS parameters

$$\tau_{\rm diss} \sim \frac{2\rho R^2}{5 \epsilon_B \epsilon_\Omega^2 \zeta} \,, \tag{16}$$

where the integral in Eq. (15) is substituted by a volume-averaged bulk viscosity times a volume-averaged rotational deformation $\epsilon_\Omega \sim \Omega^2 \sim \delta\rho/\rho$, and the NS moment of inertia as that of a uniform density sphere.

We note some implications of Eqs. 16: *i)* $\tau_{\rm diss} \sim \zeta^{-1}$: larger(smaller) values of the bulk viscosity coefficient imply a shorter(longer) dissipation time. Note that, since $\zeta \sim T^6$, the tilt angle evolution is very sensitive to the NS cooling history; *ii)* $\tau_{\rm diss} \sim \epsilon_B$, since $\zeta \sim \epsilon_B^{-2}$: the dissipation time is thus longer for larger ellipticities; *iii)* $\tau_{\rm diss} \gg T_p \approx \mathrm{P_{ms}}/(\epsilon_{B,-3} \cos\chi)$ s: damping takes a large number of cycles, unless $\chi \approx \pi/2$.

3.3 Tilt angle growth time

The growth time of the tilt angle, τ_χ, is defined as

$$\tau_\chi = \frac{\sin\chi}{\dfrac{d}{dt}\sin\chi} = \frac{\sin\chi}{\dot{\chi}\cos\chi} \tag{17}$$

from which, using the expression for E_{pre} and its time derivative, we obtain (Dall'Osso et al. 2009)

$$\tau_\chi = \frac{\sin^2\chi}{\cos^2\chi}\tau_{\rm diss}\,. \quad (18)$$

Combining these two expressions, the evolution equation for the tilt angle is readily obtained.

3.4 Tilt angle evolution

For each of the three EoS's of Sec. 2.1, and assuming a $npe\mu$ composition, we calculated the integral in Eq. 15 numerically, as described in detail by Dall'Osso & Perna (2017), *i.e.* following the change of $\Delta\rho$ described in Sec. 3.1 as the NS switches from the low-frequency to the high-frequency regime of bulk viscosity. For millisecond spin periods and ellipticities $\epsilon_B \sim 10^{-3}$, as expected in newly born magnetars, bulk viscosity enters the high-frequency regime at temperatures $\lesssim 10^{10}$ K. The resulting expressions for $\tau_{\rm diss}$ have been used to calculate the temporal evolution of χ.

3.4.1 Coupled tilt angle and spin evolution

Since $\tau_{\rm diss}$ depends on the precession frequency, hence on the NS spin, the evolution equations for χ and Ω are formally coupled. Dall'Osso et al. (2009) solved the equation for $\chi(t)$ under the assumption of a constant Ω, i.e. that spin-flip was much faster than the initial spindown due to the magnetic dipole. Here we extend their treatment, by adopting the newly derived expression for $\tau_{\rm diss}$ and solving the coupled evolution equations for $\chi(t)$ and $\Omega(t)$, without restrictions on the relation between the spin-flip and magnetic dipole spindown timescales.

3.4.2 Numerical solutions

We obtain the evolution equation for the spin frequency by considering that the NS spin energy is extracted by two mechanisms : *i)* magnetic dipole radiation - which acts right after the NS is born - at the rate (e.g., Spitkovski 2006)

$$\dot{\rm E}_{\rm EM} = -\frac{\mu^2\Omega^4}{c^3}\left(1+\sin^2\chi\right)\,, \quad (19)$$

where $\mu = {\rm B_d}R^3/2$ is the NS magnetic moment, $\rm B_d$ the dipole field strength at the magnetic pole and χ the tilt angle of the dipole field to the spin axis (assumed to be equal to the tilt of the axis of the interior toroidal field); *ii)* GW emission, at the rate (Jones & Andersson 2001)

$$\dot{\rm E}_{\rm GW} = -\frac{2}{5}\frac{\rm G}{c^5}\left(I\epsilon_B\right)^2\Omega^6\sin^2\chi\left(1+15\sin^2\chi\right)\,; \quad (20)$$

we set $\sin^2\chi\left(1+15\sin^2\chi\right) \equiv \hat{F}(\chi)$ for later use.

The differential equation for Ω will thus be

$$\dot{\Omega} = \left(\dot{\rm E}_{\rm GW}+\dot{\rm E}_{\rm EM}\right)/I\Omega. \quad (21)$$

Tilt angle distribution at $t = 10^3$ s – By combining Eqs. 21 and 18, and using Eq. 15 for $\tau_{\rm diss}$, we can calculate the numerical solutions for $\chi(t)$ and $\Omega(t)$ given the NS mass, radius, EoS (hence ζ) and initial conditions (χ_i, $\rm P_{ms,i}$, ϵ_B, $\rm B_d$). Fig. 3 illustrates results for EoS *II*, with the value of χ at $t = 10^3$ s reported as a function of the initial spin period and NS ellipticity, in three representative cases: *a)* in the top panel, a 1.4 $\rm M_\odot$ NS with a 12 km radius and $\rm B_d = 6\times10^{14}$ G are used; *b)* in the middle panel, the same mass and radius are considered, along with a much stronger dipole $\rm B_d = 5\times10^{15}$ G; *c)* the bottom panel shows results for an 1.9 $\rm M_\odot$ NS, with a 10 km radius and $\rm B_d = 6\times10^{14}$ G. Over most of the parameter space, the growth time of the tilt angle is < 20 s, and in no case it exceeds a few hundred seconds.

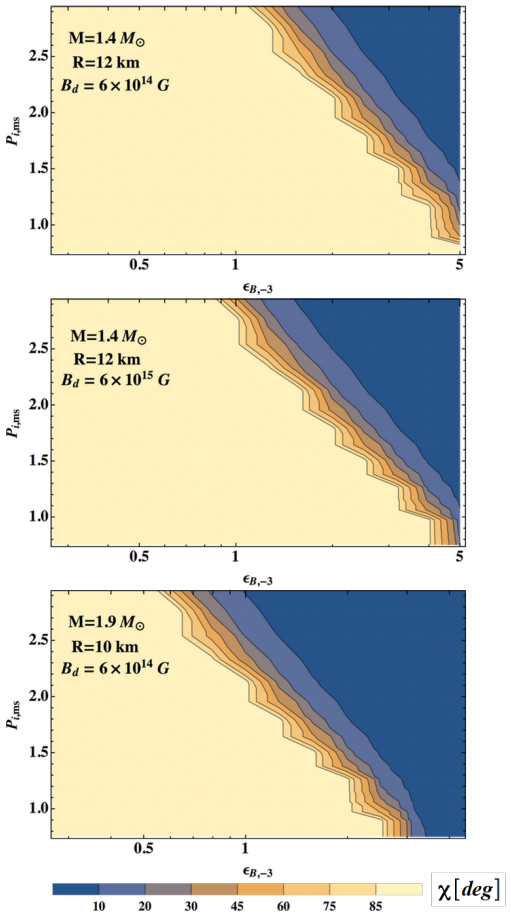

Figure 3. Tilt angle χ, calculated at $t \gtrsim 10^3$ s, as a function of the initial spin and magnetically-induced ellipticity, for EoS *II* and three different NS parameter combinations (shown in the plots). The parameter space is divided in two by a relatively narrow strip: most magnetars end up either as almost orthogonal (yellow area, left) or almost aligned (blue area, right) rotators. A larger magnetic dipole (*middle panel*) has a minor impact demonstrating that spin-flip, when it occurs, is faster than the EM spindown. A larger mass, on the other hand, effectively delays spin-flip, slightly reducing the range in parameter space occupied by large tilt angles (*lower panel*). In the upper panel, the relation $P_{\rm ms} < -3.33\log_{10}\epsilon_{B,-3} + 3.23$ approximates the dividing line at $\chi \approx 60°$. Similarly, for the middle and lower panels we obtain, respectively, $P_{\rm ms} < -3.1\log_{10}\epsilon_{B,-3} + 2.85$ and $P_{\rm ms} < -3.23\log_{10}\epsilon_{B,-3} + 2.27$.

In all panels, two regions are apparent: almost orthogonal or nearly aligned rotators, separated by a relatively narrow strip of intermediate cases. The upper and middle

panels show clearly that the separation is almost insensitive to the strength of the magnetic dipole field, confirming that spin-flip is, in general, faster than magnetic dipole spindown (Dall'Osso et al. 2009). The upper and lower panels, on the other hand, show a small, yet noticeable influence of the NS compactness: the more massive and smaller NS tends to dissipate more slowly, resulting in a slightly larger region of aligned rotators in parameter space (see caption for more details). Spin-flip fails in the high-ϵ_B and long $P_{\rm ms}$ sector of parameter space, owing to the freezing of viscous dissipation when the dissipation time is longer than the cooling time. At birth, both timescales scale as T^{-6}, so whether this condition is realized or not is determined by initial values of ϵ_B and $P_{\rm ms}$. Once the switch to the high-frequency regime of bulk viscosity has completed, $\tau_{\rm diss}$ becomes even more sensitive to T, progressively freezing the value of the tilt angle. Since, in this regime, the dissipation time is $\sim \epsilon_B$, large-ellipticity NSs are those mostly affected by the freezing.
The density-averaged bulk viscosity coefficient for EoS II is ≈ 3 times larger than the value in Eq. 2. For EoS I it is almost twice as strong, making an even larger region of parameter space accessible to orthogonal rotators. For EoS III, it is just 2/3 of the one adopted in Fig. 3, leading to a small reduction of the interesting parameter range.

4 GW & EM TRANSIENTS

The NS spin energy is $E_{\rm spin} = (1/2) I \Omega^2$. The moment of inertia can be well approximated by the polynomial[9] (Lattimer & Prakash 2016)

$$I \approx M R^2 \left(0.247 + 0.642\beta + 0.466\beta^2\right) , \qquad (22)$$

as a function of the compactness $\beta = GM/(c^2 R)$. Because the maximum NS spin frequency is also expressed by a nearly universal relation (Lattimer & Prakash 2016),

$$\nu_{\rm max} \approx 1.08 \text{ kHz } \left(\frac{M}{1.4 M_\odot}\right)^{1/2} \left(\frac{R}{10 \text{km}}\right)^{-3/2} , \qquad (23)$$

where M and R refer to the non-rotating configuration, then the maximum spin energy of a NS can be expressed, in terms of (22) and (23), as

$$E_{\rm spin,max} = 4.6 \times 10^{52} \left(\frac{M}{M_\odot}\right)^2 \left(\frac{R_*}{10 \text{ km}}\right)^{-1} \left(0.247 + 0.642\beta + 0.466\beta^2\right) \text{ erg} . \qquad (24)$$

The maximum NS mass is $\gtrsim 2\ M_\odot$ (Antoniadis et al. 2013): thus, $E_{\rm spin,max}$ can range from $\lesssim 3 \times 10^{52}$ erg, for a $M = 1.4\ M_\odot$, R= 12 km NS, to $\sim 10^{53}$ erg in extreme cases.

The two torques described in Sec. 3.4.2 draw spin energy and channel it into the EM and GW windows, respectively. Eq. 19 gives the initial spindown time due to magnetic dipole emission, $\tau_{\rm em} \sim 1.7 \text{ day } P_{i,\rm ms}^2 B_{\rm d,14}^{-2} \left(1 + \sin^2\chi\right)^{-1}$, P_i being the birth spin period. From Eq. 20 we get the GW-driven spindown time, $\tau_{\rm GW} \sim 3.3 \text{ day } P_{i,\rm ms}^4 \epsilon_B^2 \hat{F}(\chi)^{-1}$. Given the large spin energy reservoir and short timescales involved, bright EM and/or GW transients may occur when a highly magnetised, millisecond spinning NS is formed. The initial conditions determine the relative strengths of the EM and GW spindown luminosities.

The solutions for $\chi(t)$ and $\Omega(t)$ from Sec. 3.4.2 are needed in order to calculate spindown luminosities as a function of time in both the GW and EM window (Eqs. 19 and 20); in this way, it is possible characterise both types of transients and determine their detectability.

4.1 GW transient signals

Our numerical solutions for $\chi(t)$ extend the analytical results of Dall'Osso et al. (2009). On the one hand they confirm that, for a large portion of parameter space, efficient GW emission is favored by the tilt angle quickly attaining large values ($> 60^\circ$), before the NS spin energy can be drained by EM torques. On the other hand, they reveal that bulk viscous dissipation will drop faster than previously calculated, limiting the growth of the tilt angle at large ϵ_B, despite the larger bulk viscosity coefficient calculated here. In particular, if[10] $\epsilon_{B,-3} \gtrsim 5$ the tilt angle remains small and, accordingly, the GW emission efficiency has a sharp drop.

To update earlier results on the strength and detectability of the expected GW signals, we first estimate the signal-to-noise ratio (S/N) for a one-detector ideal match-filtered search (e.g. Owen & Lindblom 1998). The orientation- and position-averaged strain is (Finn & Chernoff 1993)

$$h_a^2(f) = \frac{2\pi^4 G^2 I^2 \epsilon_B^2}{5 c^8 D^2} f^4 \hat{F}(\chi) \qquad (25)$$

where $f = \Omega/\pi$ is the GW signal frequency and D the source distance. The signal-to-noise ratio is thus

$$S/N = 2\sqrt{\int \frac{\tilde{h}_a^2(f)}{S_h(f)}\, df} . \qquad (26)$$

In Eq. (26), $\tilde{h}(f)$ is the Fourier transform of the instantaneous strain, and $S_h(f)$ the one-sided noise spectral density of the detector. For Advanced LIGO/Virgo we adopted the design sensitivity curve[11] of Abbott et al. (2017b).

Detection by Advanced LIGO/Virgo – We calculated Eq. 26 in the case of EoS II, for two values of the NS magnetic moment, two combinations of the NS mass and radius, and adopting a standard distance of 20 Mpc. Results are shown in Fig. 4 (see caption for details). The GW signals last from $\sim$ a few hours up to $\gtrsim$ a day (depending on the values of $P_{\rm ms}$, ϵ_B and $B_{\rm d}$), during which the frequency decreases by a factor $\sim 2-3$. S/N-values in Fig. 4 were calculated by integrating the signals for the first 12 hrs after the NS is born. We verified that, for the weaker signals, increasing the time span up to ~ 24 hrs can result in a $\sim 25\%$ gain in S/N, while for the most powerful events the signal is concentrated in less than 12 hrs (our results are thus somewhat conservative for the lower-S/N signals).
Fig. 4 shows that a stronger $B_{\rm d}$ reduces the detectable region in parameter space and shifts it towards larger ϵ_B, as it increases the EM over the GW torque. Increasing the NS mass has a comparable effect, but shifts the detectable region to lower ellipticities. This results from the combination

[9] Valid for $\beta > 0.1$ and maximum NS mass $\geq 1.97\ M_\odot$.

[10] The exact value depending also on the NS spin.

[11] Data files from https://dcc.ligo.org/LIGO-P1200087-v42.

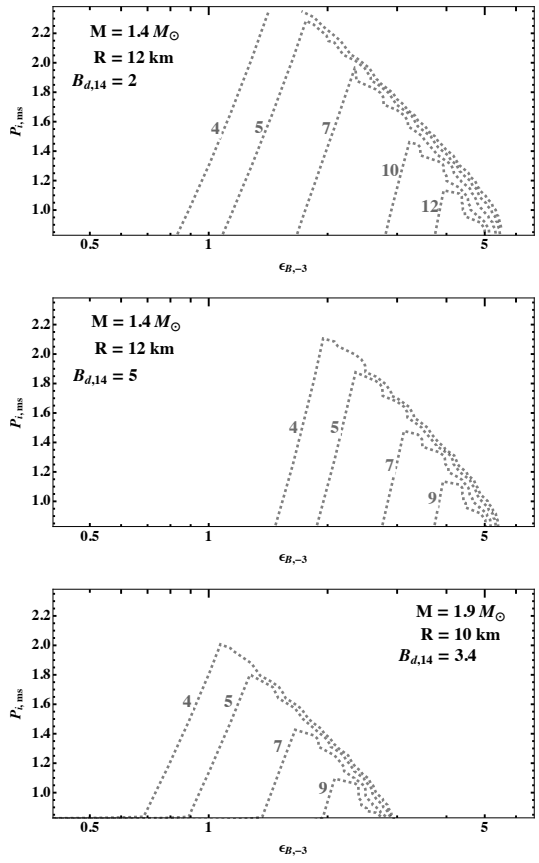

Figure 4. The orientation- and position-averaged S/N of a newborn magnetar at 20 Mpc, for EoS *II* and a single-detector matched-filter search, as a function of $P_{\rm ms}$ and ϵ_B. Signals are integrated for $\Delta t = 12$ hrs. We adopted two different values of the magnetic dipole moment and two choices of the NS mass and radius (see plots). In the upper and lower panels, the same value of $\mu_{32} = 1.7$ is used: different values of $B_{\rm d}$ reflect different NS radii. The positive slope side of the contours reflects magnetars whose tilt angle becomes quickly $\sim 90°$: they efficiently emit GWs with a strain $\propto \epsilon_B$. The negative slope side corresponds to sources in which cooling freezes spin-flip before the tilt angle becomes large: they emit GWs with lower efficiency, which drops at higher ϵ_B.

of a larger moment of inertia, which slightly favors the GW over the EM torque, and of incomplete flipping (see Fig. 3), which reduces the GW efficiency at larger ϵ_B. Finally, for a fixed value of $B_{\rm d}$, the maximum distance at which S/N is above a given threshold scales almost linearly with $1/P_{\rm i,ms}$ and ϵ_B. A sharp cut off in the maximum distance occurs for ϵ_B-values beyond the descending branch of the S/N curves in Fig. 4.

The long duration and strong spin-down of these *time-reversed* "chirps" pose new technical challenges, not fully addressed by current detection algorithms. While a complete discussion of these problems is clearly beyond the scope of this work, we summarize them here, in order to assess realistic perspectives for signal detection.

Even with match-filtering, actual signal searches with unknown phase parameters have an $\mathcal{F}$-statistics maximum S/N that is a factor $\sqrt{2}$ lower than the optimal value of Eq. 26 (Eqs. 31, 64, 112 in Jaranowski & Królak 2000). In reality, the search for these GW signals will be limited by available computing power, and will have to be carried out by using sub-optimal methods, leading to a further loss of sensitivity (e.g., Thrane et al. 2011, Prix et al. 2012, Coyne et al. 2016). In a semi-coherent search, short data sets can be analyzed coherently and then combined incoherently to increase sensitivity. However, this is less sensitive than a coherent search by a factor $\sim N^{-1/4}$, where $N = T_{\rm obs}/T_{\rm short}$ is the number of short data sets in which the whole observation is split. The potential of these methods can be enhanced in an hierarchical scheme, in which candidate events are followed up with increasingly selective criteria and a finer tiling in a smaller region of parameter space. As a specific example, we assumed a search done with the frequency Hough-transform, which extends the existing calculations for continuous waves (Astone et al. 2014) to periodic signals slowing down on a $\sim 10^4 - 10^5$ s timescale (Miller et al., in preparation). We adopted $\epsilon_{B,-3} \sim 1$, $I_{45} = 1.4$, an initial spin period of 1 ms, $T_{\rm shor} \lesssim 100$ s and standard values for (i) the threshold on the critical ratio for candidate selection on the Hough map ($\rm CR_{thr} \sim 5$), which sets the false alarm probability; (ii) the threshold for peak selection on the equalized power spectra $\theta_{\rm thr} = 2.5$ (see Astone et al. 2014). The loss in sensitivity translates into a factor $\sim$ 5-6 smaller range with respect to the value adopted in Fig. 4 (Miller et al. in preparation).

Detection by the ET – The sensitivity of third generation detectors, like the Einstein Telescope (ET), will improve significantly over that of Advanced LIGO/Virgo. In the ET-D configuration, for which $S_0 \approx 3.6 \times 10^{-49}$ Hz^{-1} at 1 kHz and the a sensitivity gain by a factor ~ 8 can be anticipated. Therefore, the curves of Fig. 4 would hold for a distance of ~ 160 Mpc, whereas taking into account the sensitivity loss of semi-coherent searches, the corresponding range would become $\sim 25 - 30$ Mpc.

Expected event rate – Millisecond spinning magnetars may be formed either in the core-collapse (CC) of massive stars or in binary NS mergers. Li et al. (2011) estimate a rate $\sim 0.7 \times 10^{-4}$ yr^{-1} Mpc^{-3} for all CC SNe in the local universe. To average out local over-densities, we integrate the rate over 60 Mpc, within which ~ 65 CC SNe per year are expected. Using the cumulative blue light distribution in the local universe (Kopparapu et al. 2008; Abadie et al. 2010) as a proxy for the star formation rate, the above translates to a magnetar birth rate of (i) $\gtrsim 0.3$ yr^{-1} within 20 Mpc, if they represent $\gtrsim 10\%$ of all NSs formed in CC SNe (note that Stella et al. 2005 estimated $\lesssim 1$ yr^{-1}, based on the energetics of magnetar Giant Flares); (ii) $\gtrsim 0.01$ yr^{-1} within 4 Mpc, the sub-optimal horizon for Advanced LIGO/Virgo; (iii) $\sim (0.5-1)$ yr^{-1} within 25-30 Mpc, the estimated range of third generation detectors.

Newborn magnetars formed in BNS mergers could either be stable objects, or supra/hyper-massive NS bound to collapse to black holes after loosing some of their centrifugal support (e.g. Giacomazzo & Perna 2013, Metzger 2017). In the latter case, their GW signals, albeit shorter lived, may be especially rich of information about the NS EoS (Dall'Osso et al. 2015; Piro et al. 2017). In the former case, the signal would be slightly stronger than calculated here - because the NS is close to the maximum mass - and

would thus allow for a somewhat larger horizon, $\lesssim 40$ Mpc with third generation detectors (adopting the numbers from Dall'Osso et al. 2015, and factoring in the sensitivity loss of realistic searches, as discussed above). The event rate for BNS mergers is estimated to be $\sim (320-4700)$ Gpc^{-3} yr^{-1} (Chruslinska et al. 2017 and references therein), implying a rate $\sim (0.9-13)\times 10^{-4}$ yr^{-1} within the sub-optimal horizon for Advanced LIGO/Virgo, and $\sim (0.09-1.3)$ yr^{-1} within the sub-optimal horizon for third generation detectors (see e.g. Dall'Osso et al. 2015, Piro et al. 2017 for a discussion of the fraction of BNS mergers that may produce stable/supramassive NSs). In the latter case, the stronger "chirp" from the inspiral would serve as a trigger for a targeted search of the signal emitted by the newly formed NS.

4.2 EM transients

The GW signals from magnetars born in CC are expected to be associated to SN explosions (e.g. Thompson & Duncan 1993, Gaensler et al. 1999). Within the ranges estimated in Sec. 4.1 for Advanced and third generation interferometers, these SNe would be easily identified in the optical/NIR. This makes prospects for multi-messenger studies of such GW events especially promising. For magnetars originating from binary NS mergers, the same two types of EM counterparts predicted for the merger are expected: a prompt, short gamma-ray burst (GRB) for favorable viewing angles (e.g. Eichler et al. 1989) and/or a kilonova on a timescale $\sim$ day, for a wide range of viewing angles (e.g., Li & Paczyński 1998, Metzger 2017; Coulter et al. 2017, Arcavi et al. 2017, Cowperthwaite et al. 2017, Kasen et al. 2017).

The NS spin energy may contribute powering the SN or other phenomena, if magnetic dipole spindown is dominant, as extensively discussed in the literature. Magnetars formed in core-collapse may lead to the production of a long-GRB (e.g. Thompson et al. 2004, Bucciantini et al. 2006, Metzger et al. 2007, 2011), a shallow decay phase in the GRB early afterglow (e.g. Zhang & Meszaros 2001, Dall'Osso et al. 2011, Bernardini et al. 2012) or a Super-Luminous Supernova (SLSN; Kasen & Bildsten 2010, Greiner et al. 2015). The spin energy of a magnetar formed in a binary NS merger may power the extended emission following (some) short GRBs (Metzger et al. 2008, 2011). The co-existence of a GW torque has not been considered yet in any of such scenarios; however, GW-driven spindown was considered by, e.g. Dall'Osso & Stella 2007 and Dall'Osso et al. 2009, in relation to the energetics of SN remnants associated to galactic magnetars. We plan to address this issue in greater detail in a future study.

5 CONCLUSIONS

We improved on previous work on the role of the spin-flip instability in the GW emission from newborn magnetars, by: a) calculating the coefficient of bulk viscosity, the dissipative process driving the instability, for $npe\mu$ matter, with various realistic EoS's; b) introducing a prescription for the way in which fluid compressibility drops as the cooling NS switches between the low- and high-frequency limits of bulk viscosity; c) deriving the first self-consistent solution of the coupled evolution equations for the NS tilt angle ("spin-flip") and spin frequency, under the effect of bulk viscous dissipation, and of GW and EM spindown torques. Based on that, we calculated the detectability of the GW signal with Advanced LIGO/Virgo and future third generation detectors, as a function of the magnetically-induced ellipticity and initial spin period of the NS.

Our main conclusions are: i) the bulk viscosity coefficient of NS matter with a realistic EoS and chemical composition is, in general, larger than the standard expression valid for pure *npe* matter. This makes bulk viscous dissipation more efficient than previously calculated, and the "spin-flip" instability accordingly faster; ii) the "spin-flip" instability freezes, and the tilt angle stops growing, as the NS cools below $\sim (8-9)\times 10^9$ K, due to the decreasing compressibility of the $npe\mu$ fluid. iii) at spin periods $\lesssim 2$ ms, spin-flip will cause a fast growth of the tilt angle χ, in turn causing strong GW emission. At large ellipticities, on the other hand, the tilt angle growth time is proportionally longer, and spin-flip freezes before χ has evolved significantly. We find that, for $\epsilon_{B,-3} \gtrsim 5$, GW emission is quenched because the tilt angle remains close to its (small) initial value; iv) in realistic data analyses with sub-optimal sensitivity, Advanced LIGO/Virgo-class detectors can capture the GW signal of a millisecond spinning, magnetically-distorted NS up to a distance $\sim (3-4)$ Mpc $\epsilon_{B,-3}/\mathrm{P_{ms}}$, provided that the dipole B-field is $\mathrm{B_d} \lesssim 3\times 10^{14}$ G. Magnetars are expected to form in $\gtrsim 10$ % of CC SNe, implying one event per $\sim$ 30-100 yrs within that distance range. v) Third-generation interferometers, with a sensitivity improved by a factor $\sim$ 8 in the relevant frequency range, will push the horizon of even sub-optimal searches to > 30 Mpc, within which an event rate $\gtrsim (0.5-1)$ yr^{-1} can be expected. In addition, this expanded horizon would likely include an interesting number of BNS mergers ($\sim 0.09-1.3$) yr^{-1} according to current best estimates), increasing the chances of detecting magnetars formed in binary NS mergers, the exact rate of which depends on the uncertain fraction of mergers that can produce a stable, or long-lived, NS.

For magnetars formed in the core-collapse of massive stars the accompanying optical/NIR SN should be easily detectable within the horizon of Advanced and third generation interferometers, leading to a robust association between the GW signal and the EM counterpart. For magnetars formed in BNS mergers, an optical/NIR kilonova emission should be expected for most viewing geometries, along with a (short) γ-ray burst for a favourable viewing angle and/or for sufficiently small distances, as the event GW170817 has demonstrated (e.g. Abbott et al. 2017e; Coulter et al. 2017, Arcavi et al. 2017; Alexander et al. 2018). The spin energy of a millisecond NS can provide additional power to the EM emission of these events, in a manner similar to that discussed for e.g. long-GRBs and SLSNe. In all cases, detection of the characteristic GW *time-reversed* "chirp" associated to a newborn magnetar would give an unambiguous confirmation of the nature of the central engine. The development of much-needed search algorithms and strategies for the detection of such signals is urged.

Acknowledgments. SD acknowledges support from NSF award AST-1616157. LS acknowledges financial contribution from agreement ASI-INAF I/037/12/0.

REFERENCES

Abbott, B. P., Abbott, R., Abbott, T. D., et al. 2016, Phys. Rev. Lett., 116, 061102
Abbott, B. P., Abbott, R., Abbott, T. D., et al. 2017a, Physical Review Letters, 118, 221101
Abbott, B. P, Abbott, R., Abbott, T. D., et al. 2017b, arXiv:1304.0670
Abbott, B. P., Abbott, R., Abbott, T. D., et al. 2017c, Classical and Quantum Gravity, 34, 044001
Abbott, B. P., Abbott, R., Abbott, T. D., et al. 2017d, Physical Review Letters, 119, 161101
Abbott, B. P., Abbott, R., Abbott, T. D., et al. 2017e, ApJ, 848, L12
Akgün, T., Reisenegger, A., Mastrano, A., & Marchant, P. 2013, MNRAS, 433, 2445
Akmal, A., Pandharipande, V. R., & Ravenhall, D. G. 1998, Physical Review C, 58, 1804
Alexander, K. D., et al. 2018, arXiv:1805.02870
Antoniadis, J., Freire, P. C. C., Wex, N., et al. 2013, Science, 340, 448
Arcavi, I., Hosseinzadeh, G., Howell, D. A., et al. 2017, Nature, 551, 64
Astone, P., Colla, A., D'Antonio, S., Frasca, S., & Palomba, C. 2014, PRD, 90, 042002
Bernardini, M. G., Margutti, R., Mao, J., Zaninoni, E., & Chincarini, G. 2012, A&A, 539, A3
Bonazzola, S., & Gourgoulhon, E. 1996, A&A, 312, 675
Braithwaite, J. 2009, MNRAS, 397, 763
Bucciantini, N., Thompson, T. A., Arons, J., Quataert, E., & Del Zanna, L. 2006, MNRAS, 368, 1717
Chruslinska, M., Belczynski, K., Klencki, J., & Benacquista, M. 2018, MNRAS, 474, 2937
Ciolfi, R., & Rezzolla, L. 2013, MNRAS, 435, L43
Corsi, A., & Mészáros, P. 2009, ApJ, 702, 1171
Coulter, D. A., Foley, R. J., Kilpatrick, C. D., et al. 2017, Science, 358, 1556
Coyne, R., Corsi, A., & Owen, B. J. 2016, PRD, 93, 104059
Cutler, C. 2002, PRD, 66, 084025
Dainotti, M. G., & Del Vecchio, R. 2017, New Astron. Rev., 77, 23
Dall'Osso, S., Shore, S. N., & Stella, L. 2009, MNRAS, 398, 1869
Dall'Osso, S., Giacomazzo, B., Perna, R., & Stella, L. 2015, ApJ, 798, 25
Dall'Osso, S., & Perna, R. 2017, MNRAS, 472, 2142
Demorest, P. B., Pennucci, T., Ransom, S. M., Roberts, M. S. E., & Hessels, J. W. T. 2010, Nature, 467, 1081
Eichler, D., Livio, M., Piran, T., & Schramm, D. N. 1989, Nature, 340, 126
Finn, L. S., & Chernoff, D. F. 1993, PRD, 47, 2198
Gaensler, B.M., Gotthelf, E.V., Vasisht, G. 1999, ApJ, 526, L37
Giacomazzo, B., & Perna, R. 2013, ApJ, 771, L26
Greiner, J., Mazzali, P.A., Kann, D.A., et al. 2015, Nature, 523, 189
Haensel, P., Levenfish, K.P., Yakovlev, D.G. 2000, A&A, 357, 1157
Haensel, P., Levenfish, K.P., Yakovlev, D.G. 2001, A&A, 372, 130
Ipser, J. R., & Lindblom, L. 1991, ApJ, 373, 213
Jaranowski, P., & Królak, A. 2000, PRD, 61, 062001
Jones, D. I., & Andersson, N. 2001, MNRAS, 324, 811
Kasen, D., & Bildsten, L. 2010, ApJ, 717, 245
Lander, S. K., & Jones, D. I. 2017, MNRAS, 467, 4343
Lasky, P. D., & Glampedakis, K. 2016, MNRAS, 458, 1660
Lattimer, J. M., & Prakash, M. 2016, Physics Reports, 621, 127
Li, L.-X., & Paczyński, B. 1998, ApJ, 507, L59
Lindblom, L., & Owen, B. J. 2002, PRD, 65, 063006
Makishima, K., Enoto, T., Hiraga, J. S., et al. 2014, Physical Review Letters, 112, 171102
Mastrano, A., Melatos, A., Reisenegger, A., & Akgün, T. 2011, MNRAS, 417, 2288
Mestel, L., & Takhar, H. S. 1972, MNRAS, 156, 419
Metzger, B. D., Thompson, T. A., & Quataert, E. 2007, ApJ, 659, 561
Metzger, B. D., Quataert, E., & Thompson, T. A. 2008, MNRAS, 385, 1455
Metzger, B. D., Giannios, D., Thompson, T. A., Bucciantini, N., & Quataert, E. 2011, MNRAS, 413, 2031
Metzger, B. D. 2017, Living Reviews in Relativity, 20, 3
Kasen, D., Metzger, B., Barnes, J., Quataert, E., & Ramirez-Ruiz, E. 2017, Nature, 551, 80
Owen, B. J., Lindblom, L., Cutler, C., et al. 1998, PRD, 58, 084020
Page, D., Geppert, U., & Weber, F. 2006, Nuclear Physics A, 777, 497
Page, D., Prakash, M., Lattimer, J. M., & Steiner, A. W. 2011, Physical Review Letters, 106, 081101
Piro, A. L., Giacomazzo, B., & Perna, R. 2017, ApJ, 844, L19
Prix, R., Giampanis, S., & Messenger, C. 2011, PRD, 84, 023007
Reisenegger, A., & Goldreich, P. 1992, ApJ, 395, 240
Steiner, A. W., Lattimer, J. M., Brown, E. F. 2010, ApJ, 722, 33
Stella, L., Dall'Osso, S., Israel, G. L., & Vecchio, A. 2005, ApJ, 634, L165
Thompson, C., & Duncan, R. C. 1993, ApJ, 408, 194
Thompson, T. A., Chang, P., & Quataert, E. 2004, ApJ, 611, 380
Thrane, E., Kandhasamy, S., Ott, C. D., et al. 2011, PRD, 83, 083004
Zhang, B., & Mészáros, P. 2001, ApJ, 552, L35